Three-Dimensional Phase-Field Investigation of Pore Space Cementation and Permeability in Quartz Sandstone

Nishant Prajapati[1], Michael Selzer[1,2], Britta Nestler[1,2], Benjamin Busch[3], Christoph Hilgers[3], and Kumar Ankit[4]

[1]Institute for Applied Materials (IAM-CMS), Karlsruhe Institute of Technology, Karlsruhe, Germany, [2]Institute for Digital Materials Science, Karlsruhe University of Applied Sciences, Karlsruhe, Germany, [3]Institute of Applied Geosciences (AGW-SGT)Karlsruhe Institute of Technology, Karlsruhe, Germany, [4]School for Engineering of Matter, Transport and Energy, Arizona State University, Tempe, AZ, USA

Abstract The present work investigates the dynamics of quartz precipitation from supersaturated formation fluids in granular media, analogous to sandstones, using a multiphase-field model. First, we derive a two-dimensional (2-D) Wulff shape of quartz from the three-dimensional (3-D) geometry and simulate the unitaxial growth of quartz in geological fractures in 2-D in order to examine the role of misorientation and crystal *c* to *a* axis ratios (*c*/*a*) in the formation of quartz bridge structures that are extensively observed in nature. Based on this sensitivity analysis and the previously reported experiments, we choose a realistic value of *c*/*a* to computationally mimic the 3-D anisotropic sealing of pore space in sandstone. The simulated microstructures exhibit similarities related to crystal morphologies and remaining pore space with those observed in natural samples. Further, the phase-field simulations successfully capture the effect of grain size on (I) development of euhedral form and (II) sealing kinetics of cementation, consistent with experiments. Moreover, the initially imposed normal distribution of pore sizes evolves eventually to a lognormal pattern exhibiting a bimodal behavior in the intermediate stages. Furthermore, computational fluid dynamics analysis is performed in order to derive the temporal evolution of permeability in numerically cemented microstructures. The obtained permeability-porosity relationships are coherent with previous findings. Finally, we highlight the capabilities of the present modeling approach in simulating 3-D reactive flow during progressive sealing in porous rocks based on innovative postprocessing analyses and advanced visualization techniques.

Correspondence to:
N. Prajapati,
nishant.prajapati@kit.edu

Citation:
Prajapati, N., Selzer, M., Nestler, B., Busch, B., Hilgers, C., & Ankit, K. (2018). Three-dimensional phase-field investigation of pore space cementation and permeability in quartz sandstone. *Journal of Geophysical Research: Solid Earth*, *123*, 6378–6396.

1. Introduction

Cementation and mechanical compaction are the main factors governing the quality of sandstone reservoirs (e.g., Oelkers et al., 1996; Paxton et al., 2002; Taylor et al., 2004; Walderhaug, 1994a, 1994b, 1996, 2000; Waugh, 1970; Worden & Burley, 2003; Worden & Morad, 2000). The authigenic cement phases (such as quartz and calcite) occlude the intergranular pore space or fractures, ultimately altering the flow pathways in sandstones (Oelkers et al., 1996). Therefore, petrophysical properties such as porosity and permeability serve as important indicators for the assessment of the reservoir quality (Ajdukiewicz & Lander, 2010; Amthor & Okkerman, 1998; dos Anjos et al., 2000; Dutton et al., 2012; Taylor et al., 2015). In deeply buried sandstones where extensive quartz cementation occurs, the formation fluids are mostly supersaturated with silica (Bjorlykke & Egeberg, 1993; Bjørlykke & Jahren, 2015; Thiry & Maréchal, 2001) and thermal conditions favor precipitation on substrate grains (Lander et al., 2008; Walderhaug, 1994a). Thermal exposure characterizes the time spent at elevated temperatures (>75°) that primarily favors syntaxial overgrowth cementation (Walderhaug, 1994b). The cements (or so-called *overgrowths*) form in optical continuity and will, if enough space is present, recreate the habit of quartz crystals. Differences in thermal exposure result in different volumes of quartz cements within similarly composed sandstones. For instance, the lower thermal exposure of less compacted Rotliegend sandstones in northern England results in a smaller amount of quartz cements and more retained porosity, shown in blue color in Figure 1a (Busch et al., 2017), as opposed to Rotliegend sandstones from northern Germany (shown in Figures 1c and 1d; Busch et al., 2018). The pore space in samples that experienced higher thermal exposure is completely occluded by quartz cements; see Figures 1c and 1d. The typical cross section of quartz crystals (hexagonal shape if cut perpendicular to the crystallographic *c* axis) can also be observed in

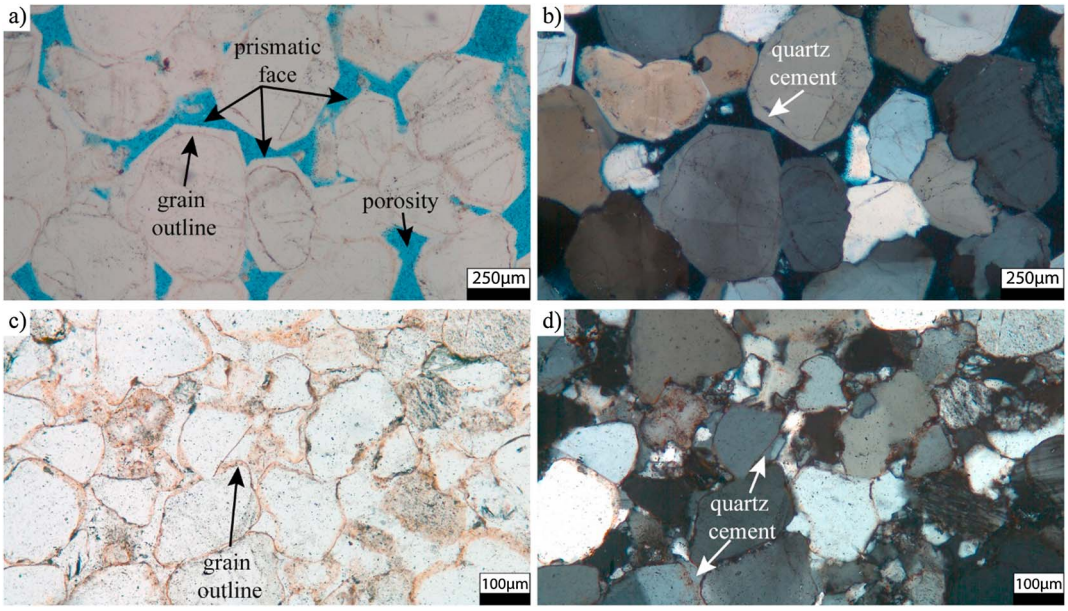

Figure 1. (a) Photomicrograph of a Rotliegendes sandstone sample from North England. Quartz cements developed crystal facets while still retaining porosity (stained with blue epoxy). The original grain outlines are visualized by the reddish-brown pigmented hematite (iron oxide) rims. (b) Photomicrograph in cross polarized light indicating the cements grew in optical continuity of the substrate grain based on the same interference color of cement and grain. (c) Photomicrograph of a Rotliegend sandstone sample from North Germany where no visible porosity is retained (no blue epoxy is visible). The original grain outlines are marked by reddish-brown pigmented hematite (iron oxide) rims. (d) Photomicrograph in cross-polarized light indicating that the complete pore space is occluded by quartz cements, grown in optical continuity on substrate grains.

syntaxial overgrowths (Figures 1a and 1b). The crystallographic orientations are inherited from the substrate grains, as indicated by the same interference colors in Figures 1b and 1d.

Sandstone being the most significant reservoir rock-type accounts for over 50% of the world petroleum reservoirs (Bjørlykke & Jahren, 2015). Therefore, diagenetic quartz cementation and its impact on porosity and permeability of sandstone has been a topic of intensive research since several decades. Empirical permeability-porosity relationships of a wide variety of rocks and influence of various evolution processes on the same have been discussed in Nelson et al. (1994), Bernabé et al. (2003), and Ma (2015). These mathematical equations act as tools to estimate permeability from porosity and other rock properties that can be derived from well logging, when core measurements are not available. On the other hand, quartz cementation models based on empirical rate laws for porosity loss in terms of physical parameters (such as initial grain size, temperature, and surface area) can also be found in literature (e.g., Canals & Meunier, 1995; Walderhaug, 1996; Wangen, 1998, 1999). Although the preceding mathematical models have been quite successful in the quantitative estimation of reservoir porosity (see ; Bjørkum et al., 1998; Lander & Walderhaug, 1999; Marchand et al., 2001; Sliaupa, 2010), they do not provide any insights into the evolving microstructures as a result of syntaxial quartz overgrowths. In order to trace the burial history and make accurate future predictions of porosity and permeability, a deep understanding of the underlying microstructural processes is imperative. Numerical approaches capable of simulating microstructure evolution and recreating morphologies observed in natural rocks are certainly advantageous.

Numerous simulation algorithms based on *front-tracking* technique have been developed (e.g., *fringe growth*, Koehn et al., 2000; *vein growth*, Bons, 2001; Hilgers et al., 2001; *facet*, Zhang & Adams, 2002) in order to simulate fracture cementation under various boundary conditions. These models with capabilities of describing grains as faceted surfaces successfully demonstrated the complicated grain boundary interactions and explained the mechanisms of formation of natural vein morphologies. However, none of the above works commented on kinetics of quartz cementation. This aspect was addressed in the work of Lander et al. (2008), who developed a solver called *Prism2D* based on *cellular automaton* approach, to simulate quartz overgrowths under a wide range of boundary conditions in realistic 2-D computational domains and validated with hydrothermal

experiments. Their experiments of undisturbed cement overgrowths on different-sized substrate grains indicated that smaller grains attained their equilibrium shape faster compared to coarser ones. Further, the numerical simulations using Prism2D confirmed the inverse dependency of quartz overgrowth kinetics on grain size of substrate. This essentially implies that sand packs with finer grains exhibit higher overall rates of quartz cementation and therefore lose porosity faster compared to coarser ones, due to the availability of higher specific surface area for overgrowths in finer packs.Despite the achievements of the aforementioned works in modeling and simulating quartz cementation, their scope has been restricted to 2-D owing to high computational costs and modeling complexities arising in 3-D. However, 2-D numerical studies offer a limited understanding of the complicated and rich phenomenon of grain growth in response to cementation, as the process involves curvatures in all spatial directions of the evolving grain boundaries. Consequently, the microstructural properties and dynamic relations are different in 3-D when compared to 2-D. Further, the shortcomings become highly evident in the estimation of permeability in porous rocks that requires information of flow pathways in full 3-D space. Computed microtomography and digital geometry processing (e.g., Auzerais et al., 1996; Blunt et al., 2013; Deng et al., 2015; Spanne et al., 1994) for numerically reconstructing 3-D pore geometries from the thin section of rock samples can only be utilized to estimate the transport properties in specific core samples. On the other hand, process-based approaches (Bosl et al., 1998; Øren & Bakke, 2002) that explicitly modeled diagenetic cementation and analyzed its implications on the evolution of permeability do not take into account the microscopic changes that occur due to anisotropic growth of cements leading to faceted crystal morphologies.

The *phase-field* method, broadly used in the material science community for modeling microstructure evolution accompanying phase transitions (e.g., review articles; Chen, 2002; Moelans et al., 2008; Nestler & Choudhury, 2011; Qin & Bhadeshia, 2010), has recently emerged as a powerful computational approach for modeling anisotropic cement overgrowths in calcite (Prajapati et al., 2018) and quartz veins (Ankit et al., 2013, Ankit, Selzer, et al., 2015, Ankit, Urai, & Nestler, 2015; Wendler et al., 2015). These works provide a basis for an entirely new generation of cementation models for sedimentary basins. The reason for increasing popularity of phase field over conventional front-tracking methods lies in the elegance with which it treats moving boundary problems by obviating the need of tracking interfaces explicitly, making it a versatile and computationally efficient approach. Extensions to combine the microstructure modeling core part of the phase-field approach with the computational fluid dynamics (CFD) have been applied to the coupled growth and fluid flow problems (e.g., Feng et al., 2017; Kling et al., 2017; Wang et al., 2012). In the present work, we employ a thermodynamically consistent *multiphase-field* model available in the simulation framework (Pace3d, 2015) to investigate the dynamics of cement overgrowths (in 3-D) from supersaturated solution in quartz sandstone. To begin with, we simulate the unitaxial evolution of quartz in geological fractures (in 2-D) and investigate the role of misorientation and crystal c to a axis ratio (c/a) in the formation of crystal morphologies in open fractures (i.e., quartz bridges) that are extensively observed in nature. Based on this sensitivity analysis, we calibrate the crystal c/a for 3-D simulations and perform a systematic study of anisotropic sealing of pore space and implications on pore size statistics in sandstone. Using CFD analysis, we then obtain the temporal evolution of permeability in partially sealed microstructures. Using the porosity and permeability data obtained from phase-field and fluid flow simulations, we derive time-dependent permeability-porosity relationships for the numerically cemented microstructures and finally compare the obtained results with the empirical *Timur's* model of permeability estimation (Timur, 1968).

2. Methods

The multiphase-field model used in the present work has been previously employed by Ankit, Selzer, et al. (2015), Ankit, Urai, and Nestler (2015), and Wendler et al. (2015) to address the problem of mineral growth in quartz veins. For the sake of completeness, the model equations describing cementation are recapitulated in section 2.1. For a detailed discussion of the general formulation of the phase-field models with applications to a wide spectrum of phase transitions and microstructure evolution processes along with numerical implementation of model equations, motivated readers are referred to the works of Stinner et al. (2004) and Nestler et al. (2005). In order to determine the flow behavior of the progressively sealed microstructures, CFD analysis was performed. The governing equations and applied boundary conditions for the flow simulations are discussed in section 2.2.

2.1. Multiphase-Field Model

We consider a domain $\Omega \subset \mathbb{R}^d, d \in \{1,2,3\}$ comprising $N \in \mathbb{N}$ different phases or grains of different orientations that are defined by a set of so-called phase-field parameters $\boldsymbol{\phi}(\mathbf{x},t) = \{\phi_1(\mathbf{x},t), \ldots, \phi_N(\mathbf{x},t)\}$. Each phase-field parameter $\phi_\alpha : \Omega \times \mathbb{R}_0^+ \to [0,1]$ describes the presence of phase $\alpha \in \{1,2,\ldots,N\}$ at position $\mathbf{x} \in \Omega$ and time $t \in \mathbb{R}_0^+$ under the summation constraint $\sum_{\alpha=1}^{N} \phi_\alpha = 1$. The region occupied by single phase α is known as α *bulk* given by $\mathcal{B}^\alpha = \{\mathbf{x} \in \Omega | \phi_\alpha(\mathbf{x},t) = 1\}$. Therefore, the total bulk region of the system can be written as $\mathcal{B} = \cup_{\alpha \in \mathbb{N}} \mathcal{B}_\alpha$. The surfaces between two or more phases are characterized by a diffuse region given by $\mathcal{I}_\Omega = \Omega \backslash \mathcal{B}$. The binary interface of phases α and β is represented by $\mathcal{I}_{\alpha\beta} := \{\mathbf{x} \in \mathcal{I}_\Omega | \phi_\alpha(\mathbf{x},t) + \phi_\beta(\mathbf{x},t) = 1\}$. The model is based on local minimization of the *Helmholtz free-energy functional* given by

$$\mathcal{F}(\boldsymbol{\phi}) = \int_\Omega \left[\left(\varepsilon a(\boldsymbol{\phi}, \nabla\boldsymbol{\phi}) + \frac{1}{\varepsilon} w(\boldsymbol{\phi}) \right) + f(\boldsymbol{\phi}) \right] \mathrm{d}\Omega, \tag{1}$$

where $\varepsilon a(\boldsymbol{\phi}, \nabla\boldsymbol{\phi})$, $\frac{1}{\varepsilon} w(\boldsymbol{\phi})$, and $f(\boldsymbol{\phi})$ denote the gradient-type, the potential-type, and the bulk free-energy density, respectively. The scalar quantity ε represents the length scale parameter that controls the width of the diffuse interface. The value of length scale parameter ε should be chosen such that the diffuse region is resolved by sufficient number ($\sim$10) of grid points. The first two terms in the right-hand side of equation (1) collectively represent the interfacial energy density contribution of the system.The *gradient energy density* acts as an energy penalty due to the formation of diffuse interfaces and is given by

$$\varepsilon a(\boldsymbol{\phi}, \nabla\boldsymbol{\phi}) = \varepsilon \sum_{\substack{\alpha,\beta=1 \\ (\alpha<\beta)}}^{N,N} \gamma_{\alpha\beta} a_{\alpha\beta}^2(\boldsymbol{\phi}, \nabla\boldsymbol{\phi}) |\mathbf{q}_{\alpha\beta}|^2, \tag{2}$$

where $\gamma_{\alpha\beta}$ denotes the surface energy of the α-β interface. Scalar function $a_{\alpha\beta}(\boldsymbol{\phi}, \nabla\boldsymbol{\phi})$ accounts for the surface energy anisotropy of α-β interface and is elaborated in section 2.1.1. The quantity $\mathbf{q}_{\alpha\beta} = \phi_\alpha \nabla\phi_\beta - \phi_\beta \nabla\phi_\alpha$ represents a generalized gradient vector, orthogonal to the α-β interface. The potential energy density contribution creates a barrier for the spontaneous phase transitions in the absence of interfacial driving forces. For the present work, we chose a *multi-obstacle potential energy density* of the form

$$\frac{1}{\varepsilon} w(\boldsymbol{\phi}) = \begin{cases} \frac{16}{\varepsilon\pi^2} \sum\limits_{\substack{\alpha,\beta=1 \\ (\alpha<\beta)}}^{N,N} \gamma_{\alpha\beta}\phi_\alpha\phi_\beta + \frac{1}{\varepsilon} \sum\limits_{\substack{\alpha,\beta,\delta=1 \\ (\alpha<\beta<\delta)}}^{N,N,N} \gamma_{\alpha\beta\delta}\phi_\alpha\phi_\beta\phi_\delta & \text{if } \boldsymbol{\phi} \in \mathcal{G}, \\ \infty & \text{else} \end{cases} \tag{3}$$

with Gibbs simplex $\mathcal{G} = \{\boldsymbol{\phi} | \sum_{\alpha=1}^{N} \phi_\alpha = 1 \text{ and } \phi_\alpha \geq 0\}$. The higher-order term ($\propto \gamma_{\alpha\beta\delta}$) in equation $(3)_1$ is constructed as a modeling term in order to avoid the occurrence of spurious third- or higher-order phases in the binary interfaces. The *bulk free-energy density* is defined as an interpolation of the free-energy densities of bulk phases given by

$$f(\boldsymbol{\phi}) = \sum_{\alpha=1}^{N} f_\alpha h(\phi_\alpha), \tag{4}$$

where f_α is the free-energy density corresponding to phase α and $h(\phi_\alpha)$ is the interpolation function that satisfies $h(0) = 0$ and $h(1) = 1$. In the present work, we chose $h(\phi_\alpha) = \phi_\alpha^3(6\phi_\alpha^2 - 15\phi_\alpha + 10)$. The difference in free-energy densities $\Delta f_{\alpha\beta}$ between two phases α and β creates a driving force for the interfaces.The evolution of each phase-field ϕ_α is derived from the variational derivative of the Helmholtz free-energy functional, given by

$$\tau\varepsilon \frac{\partial\phi_\alpha}{\partial t} = -\frac{\delta\mathcal{F}}{\delta\boldsymbol{\phi}} - \lambda, \tag{5}$$

which ensures that the free-energy decreases monotonically with time. The Lagrange multiplier λ guarantees that the summation constraint $\left(\sum_{\alpha=1}^{N} \phi_\alpha = 1\right)$ is locally sustained. In order to account for disparate kinetic coefficients ($\tau_{\alpha\beta}$) for different binary interfaces, we choose the kinetic coefficient τ proposed in Vondrous et al. (2014) of the form

$$\tau = \frac{\sum\limits_{\substack{\alpha,\beta=1 \\ (\alpha<\beta)}}^{N,N} \tau_{\alpha\beta}\phi_\alpha\phi_\beta}{\sum\limits_{\substack{\alpha,\beta=1 \\ (\alpha<\beta)}}^{N,N} \phi_\alpha\phi_\beta}. \tag{6}$$

Table 1
Nondimensional and Dimensional Values (in SI Units) of the Phase-Field Parameters Used in Simulations

Parameter	Nondimensional value	Dimensional value
Grid size Δx	1.0	1μm
Time step width Δt	0.07	81 s
Surface energy density $\gamma_{\alpha\beta}$	1.0	0.36 J/m^2
Higher-order parameter $\gamma_{\alpha\beta\delta}$	10.0	3.6 J/m^2
Length scale parameter ε	6.5	6.5μm
Kinetic coefficient of grain-liquid interface $\tau_{g,l}$	1.0	4.18×10^{14} J-s/m^4
Kinetic coefficient of grain-grain interface $\tau_{g,g}$	100.0	4.18×10^{16} J-s/m^4
Driving force $\Delta f_{g,l}$ for crystallization	−0.3	-10^5 J/m^3

Substitution of equation (1) in equation (5) yields the following system of partial differential equations:

$$\tau\varepsilon\frac{\partial\phi_\alpha}{\partial t} = \varepsilon\left(\nabla\cdot\frac{\partial a(\boldsymbol{\phi},\nabla\boldsymbol{\phi})}{\partial\nabla\phi_\alpha} - \frac{\partial a(\boldsymbol{\phi},\nabla\boldsymbol{\phi})}{\partial\phi_\alpha}\right) - \frac{1}{\varepsilon}\frac{\partial w(\boldsymbol{\phi})}{\partial\phi_\alpha} - \frac{\partial f(\boldsymbol{\phi})}{\partial\phi_\alpha} - \lambda; \quad \text{for } \alpha = 1\ldots N \tag{7}$$

with

$$\lambda = \frac{1}{N}\sum_{\alpha=1}^{N}\varepsilon\left(\nabla\cdot\frac{\partial a(\boldsymbol{\phi},\nabla\boldsymbol{\phi})}{\partial\nabla\phi_\alpha} - \frac{\partial a(\boldsymbol{\phi},\nabla\boldsymbol{\phi})}{\partial\phi_\alpha}\right) - \frac{1}{\varepsilon}\frac{\partial w(\boldsymbol{\phi})}{\partial\phi_\alpha} - \frac{\partial f(\boldsymbol{\phi})}{\partial\phi_\alpha}, \tag{8}$$

which is solved using forward Euler scheme for temporal derivative and second-order accurate central difference scheme for the spatial derivatives. The equations are efficiently implemented in a highly parallelized simulation framework called Pace3d (2015), written in language C. The general structure of the implemented framework, its parallelization, and various optimization techniques have been discussed in Hötzer et al. (2018). The phase-field simulations were performed using the nondimensional parameters listed in column 2 of Table 1. These values can very well be mapped onto the real physical values corresponding to quartz sandstone and vein systems (Okamoto et al., 2010; Okamoto & Sekine, 2011; Wendler et al., 2015) listed in column 3 of Table 1. For the sake of convenience, all the results are reported as nondimensional values.

2.1.1. Modeling Quartz Cements

Quartz crystals exhibit a wide range of growth habits depending upon the geochemical and physical growth conditions. However, prismatic habit with facets $(10\bar{1}1)$, $(01\bar{1}1)$, and $(10\bar{1}0)$ is the most common morphology observed in nature (Frondel, 1962; Rykart, 1995); see Figure 2a. In order to model such faceted crystals with sharp edges and corners, we define a strongly anisotropic faceted-type surface energy using the following piecewise function

$$a_{\alpha\beta}(\boldsymbol{\phi},\nabla\boldsymbol{\phi}) = \max_{1\le k\le n_{\alpha\beta}}\left\{\frac{\mathbf{q}_{\alpha\beta}}{|\mathbf{q}_{\alpha\beta}|}\cdot\boldsymbol{\eta}_{k,\alpha\beta}\right\}, \tag{9}$$

where $\{\boldsymbol{\eta}_{k,\alpha\beta}|k = 1,\ldots,n_{\alpha\beta}\}$ are the position vectors corresponding to the $n_{\alpha\beta}$ corners of the Wulff shape of the α-β interface. Therefore, the above surface energy anisotropy formulation provides a general framework for modeling faceted crystals of arbitrary shapes in 2-D as well as 3-D. For the 2-D numerical studies, 2-D Wulff shapes of quartz, namely, *left handed*, *symmetric*, and *right handed* (see Figure 2b), are derived (sliced out) from the 3-D geometry, by adopting the approach of Ankit, Urai, and Nestler (2015). Upon slicing the 3-D structure parallel to the *c* axis, the 2-D slice where the axes ratio was found to be the maximum was chosen for 2-D simulations.

For validation of the faceted-type anisotropy formulation of the interfacial energy function that corresponds to right-handed 2-D slice, we evolve an initially spherical grain dispersed in liquid to its precise equilibrium shape (see Figure 2c), using volume preservation algorithm of Nestler et al. (2008). Contour plots of the phase-field parameter that corresponds to grain boundary are shown in Figure 2d. The plots illustrate the evolution of an initially sharp grain-liquid interface at $t = 0$, to a smooth one at $t = 4,305$ when the grain attains its euhedral form.

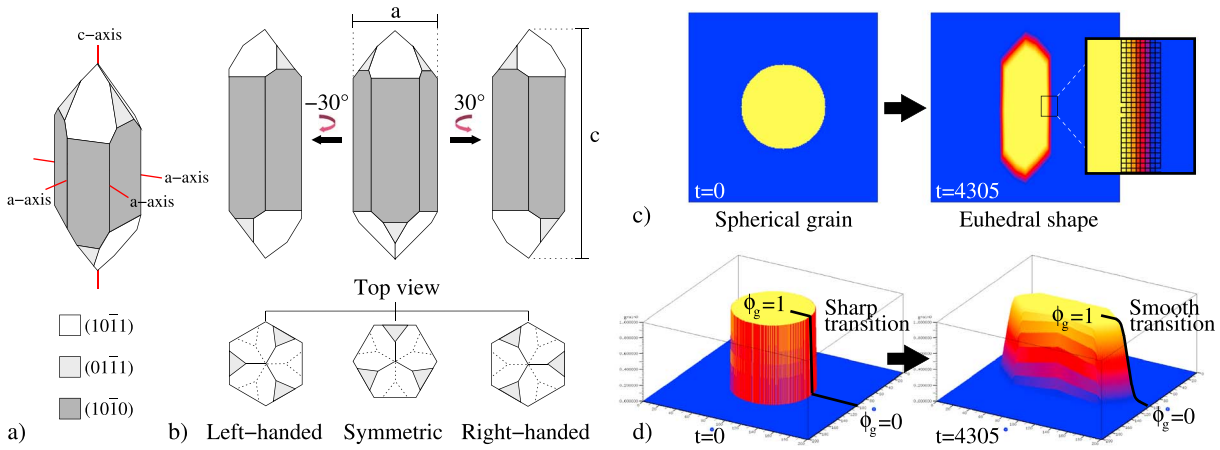

Figure 2. (a) Euhedral geometry of quartz crystal corresponding to prismatic habit with one *c* axis and three *a* axes. Different facet types are represented in different shades of gray.(b) Schematics demonstrating the method of obtaining 2-D slices from 3-D geometry. (c) Validation of the faceted-type anisotropy for studying unitaxial quartz overgrowths in fractures in 2-D. An initially spherical grain (in yellow) dispersed in a liquid phase (in navy blue) evolves to its equilibrium shape, that is, right-handed 2-D slice of quartz, while maintaining a constant volume. The zoomed outlet picture depicts the diffuse interface region consisting of finite number of discretization grid points. (d) Contour plots illustrating the sharp grain-liquid interface at $t = 0$ and the diffuse interface of the euhedral shape at $t = 4,305$, due to interfacial energy density contribution. The phase-field parameter of grain ϕ_g varies smoothly from $\phi_g = 0$ in liquid to $\phi_g = 1$ in the bulk region of the grain.

2.2. CFD: Estimation of Permeability

In order to determine potential flow behavior of the progressively cemented microstructures, CFD technique is employed. CFD simulations are performed for different stages of cementation based on the 3-D microstructural data extracted from phase-field simulations. Flow in the pore space is described by incompressible, viscous fluids and laminar flows. The governing laws of momentum and mass balance are described by the classical Stokes' equations that reads

$$\begin{aligned} \mu\Delta\mathbf{u} - \nabla p + \mathbf{f} = \mathbf{0} \quad &\text{(momentum balance)} \\ \nabla \cdot \mathbf{u} = 0 \quad &\text{(mass balance)} \end{aligned} \tag{10}$$

where μ denotes the dynamic viscosity, $\mathbf{u}$ represents the fluid velocity, p is the flow pressure, and $\mathbf{f}$ is the body force. For a given pressure drop, the velocity field is calculated using *do-nothing* (or free-stream) boundary conditions (Rannacher, 2008) given by

$$p - \mu\partial_n u_n|_{S_i} = P_i, \qquad \partial_n u_\tau|_{S_i} = 0, \tag{11}$$

where S_i denotes the plane section where pressure P_i is prescribed and u_n and u_τ represent the normal and tangential components of fluid velocity with respect to S_i. All grain phases in the phase-field microstructural data are rendered stationary, and no-slip boundary conditions are applied at the grain-liquid interfaces, given by

$$\mathbf{u}|_{\text{interface}} = \mathbf{0}. \tag{12}$$

The equation for calculation of permeability (k) from the computed velocity field reads

$$k = \frac{\mu\bar{v}}{\partial p/\partial x}. \tag{13}$$

Equation (13) is a rearranged form of Darcy's law where $\bar{v}$ represents the mean velocity within the simulation domain and is given by

$$Q = A\bar{v}, \tag{14}$$

where Q represents the volumetric flow rate and A is the area of cross section. The model equations are solved using finite differences on a staggered grid system; see Harlow and Welch (1965), for example .

3. Results and Discussion

3.1. Unitaxial Growth in Fractures: 2-D Study

In order to calibrate the crystal geometry for the phase-field model of quartz cementation in sandstones, the correct ratios for growth along different axes need to be constrained. For determining the precise habit of

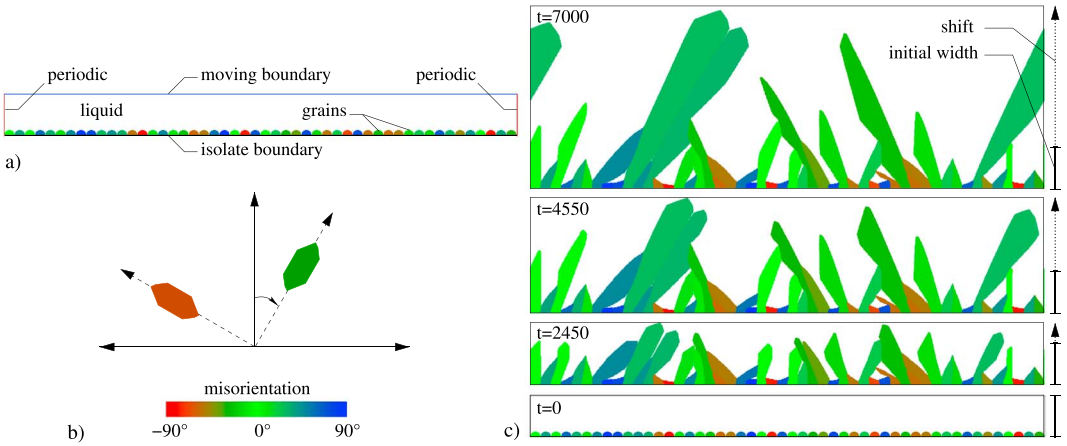

Figure 3. (a) Simulation domain consisting of 50 randomly oriented quartz grains (in RGB colors) and liquid (in white), along with the applied boundary conditions at the edges. (b) Schematics illustrating the definition of misorientation of grains. (c) Simulated unitaxial growth of quartz grains in fracture for $c/a = 3$. Dotted lines (with arrow head) indicate the shift from initial width due to moving boundary condition on the upper edge. Progression is shown at representative time steps.

quartz overgrowths, the crystal *c* to *a* axis ratios (*c*/*a*) have been previously calibrated based on laboratory synthesis of undisturbed quartz overgrowths in fractures (e.g., Lander & Laubach, 2015; Lander et al., 2008; Okamoto & Sekine, 2011). Quartz-bridge structures are known to occur extensively in natural crack-seal veins (Laubach et al., 2004) and have been discussed in the numerical works of Ankit, Urai, and Nestler (2015), Lander and Laubach (2015), and Wendler et al. (2015). By recreating these bridge morphologies in open fractures through numerical experiments of quartz growth on randomly oriented substrate grains for different values of *c*/*a* ratio, correlation to previously presented examples (Lander & Laubach, 2015; Okamoto & Sekine, 2011) can be achieved.

3.1.1. Numerical Setup

We simulate the unitaxial quartz growth in 2-D open space that characterizes a geological fracture, in order to investigate the role of crystal c/a ratio and *c* axis orientations in the formation of bridge structures in crack-seal veins. We consider a simulation domain of size $2,500\Delta x \times 200\Delta x$ comprising 50 randomly oriented spherical grains in contact with liquid phase and apply the boundary conditions shown in Figure 3a. We define the *misorientation* of each grain with respect to vertical axis, determined by the color map shown in Figure 3b. This essentially implies that grains that have *c* axis orientation normal to fracture surface are colored green and assume zero misorientation. Blue and red grains with *c* axis along the fracture surface possess the misorientations of 90° and −90°, respectively. The upper edge of the simulation domain is rendered as a *moving boundary* using a *shifting algorithm*. The algorithm activates as soon as an overgrowth reaches the upper edge and generates new layers of grid cells filled with liquid phase at successive time steps. This feature leads to time-dependent increments in the width of simulation domain. Shifting algorithm enables us to simulate unitaxial overgrowths in fractures in a computationally efficient manner by imparting flexibility in the choice of domain width. The driving force for 2-D simulations is scaled by a factor of 1/2, in order to establish equivalence in the kinetics (see ; Plapp, 2012). Therefore, with a driving force $\Delta f_{g,l} = -0.15$ for overgrowth and faceted surface energy anisotropy (corresponding to the geometry of right-handed 2-D slice of quartz), simulations were performed for different values of crystal *c*/*a* ratio, keeping the chosen misorientations (determined by the color map in Figure 3b) and other simulation parameters, as listed in Table 1, identical. The crystal *c*/*a* for different simulations was varied by changing the position vectors $\boldsymbol{\eta}_{k,\alpha\beta}$ (in the anisotropic faceted-type surface energy, section 2.1.1) of the Wulff shape such that angles between the crystal faces remain constant. Different stages of unitaxial growth (corresponding to $c/a = 3.0$) along with a temporal increase in domain width (= initial width + shift) are shown in Figure 3c, demonstrating the utility of shifting algorithm.

3.1.2. Influence of Crystal *c* to *a* Axis Ratio

We analyze the simulated quartz overgrowth at $t = 7,000$ for different values of *c*/*a* ratio; see Figures 4a–4f. It is observed that for a small *c*/*a* ratio (= 1.05), a distinct grain-liquid *growth front* evolves regardless of the chosen misorientations, and the obtained domain width (at $t = 7,000$) is small. At larger *c*/*a* ratios, the

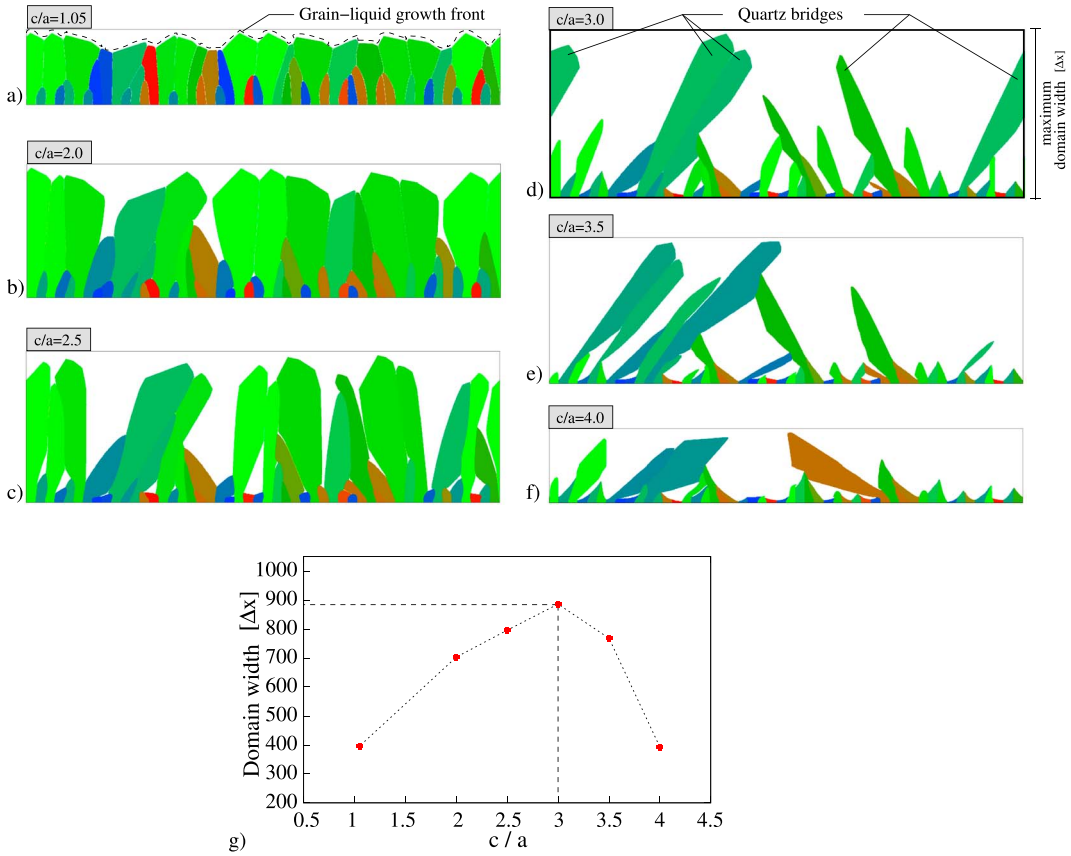

Figure 4. (a–f) Simulated unitaxial growths (until $t = 7,000$) for different values of c/a ratios. For $c/a = 1.05$, a grain-liquid growth front is observed. For $c/a = 3.0$, the domain width is maximum and is accompanied by the formation of quartz bridges. (g) Plot of domain width [Δx] over c/a for the simulations reported in Figures 4a–4f.

growth competition among the crystals as well as the domain width increases. Domain width is a measure of maximum length of overgrowth in simulations and signifies the fracture spanning potential of the evolving crystals. For $c/a = 3.0$, the tendency of leading crystals to form bridges is found to be intense, accompanied by maximum in domain width. Upon further increasing the c/a ratio, domain width as well as the crystal bridging reduces. Figure 4g depicts the plot of domain width over c/a (in red bullets) obtained from the simulations, domain width being maximum corresponding to $c/a = 3.0$. In the experimental work pertaining to unconstrained cement growth on quartz seeds, Lander et al. (2008) measured the precise growth rate ratios of the noneuhedral c and a axis growth surfaces as 1 and 0.31, respectively, resulting in $c/a \approx 3.2$. Moreover, Okamoto and Sekine (2011) separately synthesized syntaxial quartz veins through hydrothermal experiments and found that aspect ratio of well-grown crystals bridging the crack averaged at 2.9, irrespective of the variations in grain size. Our 2-D simulations of free growth with different c/a axes ratios provide a fair understanding of its influence on the bridge-forming tendency in quartz veins. Based on the presented simulations, we can infer that the best bridges are obtained in the range of 2.9 and 3.2, which is in fair agreement with previous findings of Okamoto and Sekine (2011) and Lander et al. (2008). Further, after carefully analyzing different stages of unitaxial growth for $c/a = 3.0$ as shown in Figure 3c, we deduce that during initial stages, the growth competition is not intense but temporally increases as evident in the later stages from the overgrowth of less misoriented (greenish) grains over the highly misoriented (reddish and bluish) ones, eventually resulting in the formation of well-defined quartz bridges. These results are in qualitative agreement with experimentally synthesized quartz veins (Okamoto & Sekine, 2011) as well as natural samples (Ukar et al., 2016), both of whom reported that bridging crystals were commonly oriented subnormal to the vein wall. Based on inferences drawn from the numerical studies and correlations with previous findings, it is reasonable to choose $c/a = 3.0$ for the 3-D phase-field modeling of quartz cementation in sandstones, presented in forthcoming sections.

Table 2
Numerical Values of Initial Grain Size r and Corresponding Simulation Domain Size for Unconstrained Single Crystal Growth

Grain	Grain size r	Domain size
Fine	$20\Delta x$	$200\Delta x \times 200\Delta x \times 200\Delta x$
Coarse	$40\Delta x$	$400\Delta x \times 400\Delta x \times 400\Delta x$

3.2. Cementation in Quartz Sandstone: 3-D Study

Experimental evidences have shown that development of crystal facets of quartz from a given initial grain geometry is strongly dependent on the grain size (Lander et al., 2008). That is, finer grains attain their equilibrium shape faster compared to coarser ones because overgrowth volume required to reach the euhedral form is proportional to the initial grain size. Furthermore, finer grained samples are cemented (and thereby lose porosity) faster compared to coarser sands, when the influx of cementing solution is identical in both cases (see ; Heald & Renton, 1966; Lander et al., 2008), due to the greater specific surface area available for cementation in finer grains. For a sound qualitative estimation of the influence of quartz cementation on porosity and permeability in sandstone, the present phase-field approach should be able to reproduce the aforementioned size effects while recreating the morphologies observed in natural samples.

3.2.1. Development of Crystal Facets: Undisturbed Cement Growth

As a model test case, we simulate the unconstrained cement growth on single quartz grain for two different grain sizes (r). For convenience, we address the two grain sizes as fine and coarse. For the chosen r and the corresponding domain sizes (numerical values shown in Table 2), the initial volume fraction of liquid (f_0) stays equal in each case, thereby facilitating comparison for different values of r. Under identical growth conditions, that is, equal driving forces of $\Delta f_{g,l} = -0.3$ and faceted anisotropy, simulations were performed. We analyze the crystal isosurfaces of the grains after the same time period of $t = 175$, as shown in Figure 5. The color map at $t = 175$ describes the curvature κ of isosurfaces and is calculated as $\kappa = \nabla \cdot (\mathbf{q}_{\alpha\beta}/|\mathbf{q}_{\alpha\beta}|)$.

It is evident that the fine grain with sharp (reddish) edges and corners (yellowish) has attained its euhedral form, whereas the coarse grain with blunt (flat bluish) edges and corners requires further time steps. Moreover,

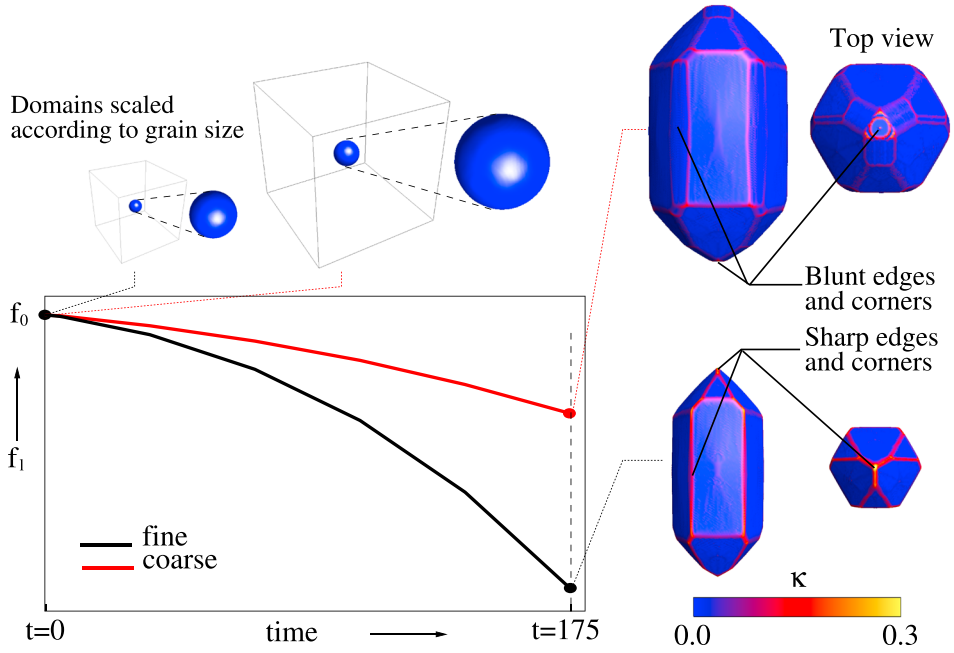

Figure 5. Plot of liquid volume fraction f_l over time for the simulated unconstrained growth for fine and coarse grains. The domain sizes are scaled corresponding to the initial grain sizes to ensure equal initial volume fraction of liquid for the two cases. The color map corresponds to curvature κ of isosurfaces of fine and coarse grains after the time $t = 175$. The fine grain develops euhedral form with flat facets and sharp edges and corners, while coarse grain has blunt edges and corners and requires more time steps to attain fully euhedral shape.

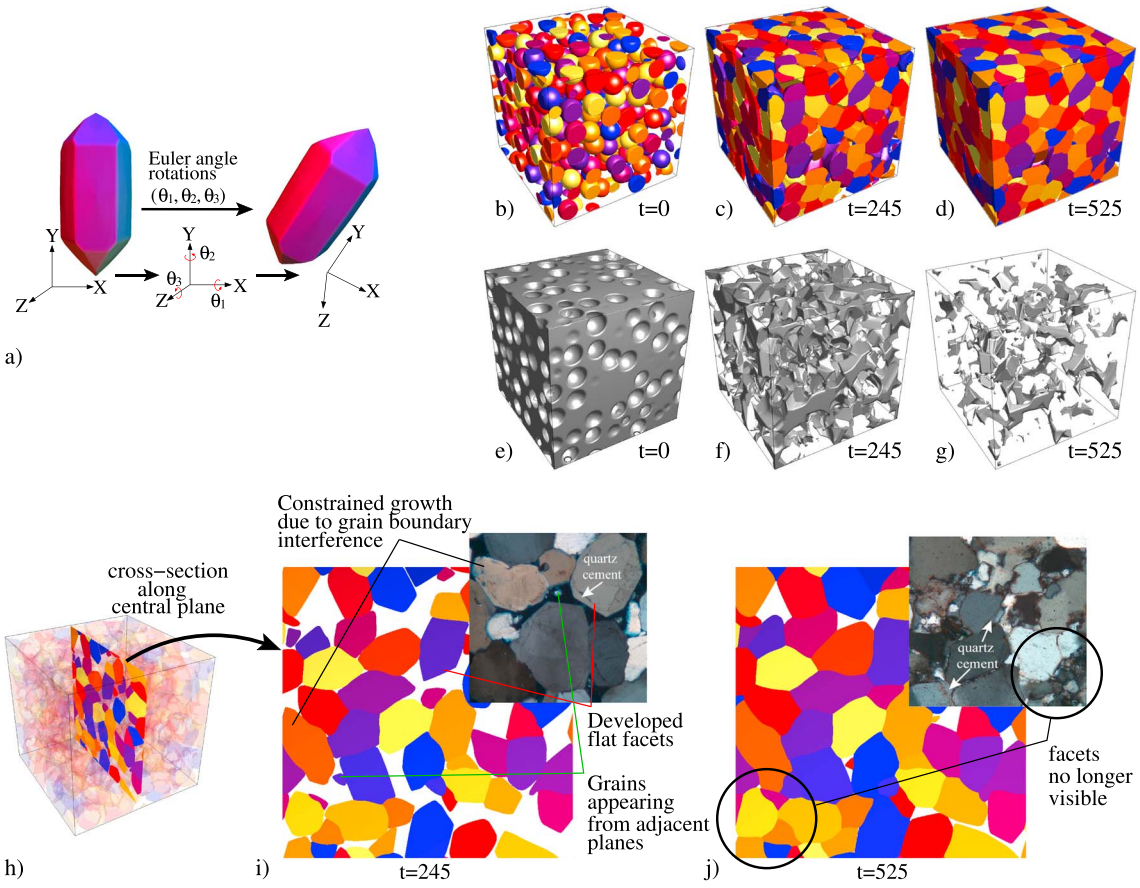

Figure 6. (a) Schematics illustrating the Euler angle rotations of a quartz crystal for assigning random crystallographic orientation to each grain of the multigrain system. Distinct colors of facets are for the sake of visualization and represent the normal direction of each facet. (b–d) Simulated quartz cementation (in BRY colors) in multigrain system. The colors are only meant to differentiate between different grains. (e–g) Simulated loss of pore space (in gray scale) in response to cementation. Progression is shown at representative time steps. (h) Visualization along the central plane of 3-D domain for comparison with thin sections of natural samples (Busch et al., 2017). (i) At $t = 245$, following similarities in patterns between simulation result and natural sample (in outlet picture) can be observed—(I) constrained growth due to grain boundary interference leading to random shapes, (II) development of flat facets (euhedral form) when enough pore space is available for growth, (III) appearance of grains from adjacent planes, as highlighted with green lines. (j) When most of the pore space is occluded by cements, the flat facets are no longer visible in simulation (at $t = 525$) as well as in thin section, indicated in black circles.

the rate of loss of liquid (indicated by temporal evolution of liquid volume fraction f_l in Figure 5) is faster for the fine grain, signifying that finer grains attain euhedral shape more rapidly compared to the coarser ones, as reported by Lander et al. (2008). In the present phase-field approach, the crystal facets are modeled as isosurfaces that evolve such that the overgrowth volume increases with every successive time step. The applied chemical driving force $\Delta f_{g,l}$ is significantly larger than the opposing curvature-driven force (see Plapp, 2012, for fundamentals of phase field). Thus, the increment in surface evolution is nearly independent of grain size. As overgrowth volume required to establish the equilibrium shape is larger for coarse grains, they require more time to recover the euhedral form.

3.2.2. Development of Crystal Facets: Growth in Multigrain System

A cubic computational domain (size, $300\Delta x \times 300\Delta x \times 300\Delta x$) consisting of 265 randomly oriented spherical nuclei (grain size $r = 20\Delta x$) is generated using the *distribution generating algorithm* described in Prajapati et al. (2017). Crystallographic orientation of each grain is defined by randomly chosen Euler angle rotations (θ_1, θ_2, and θ_3), as shown in Figure 6a. Numerical simulations were performed assuming a constant driving force of $\Delta f_{g,l} = -0.3$. Different stages of quartz cementation (in BRY colors) and pore space evolution (in gray scale) are depicted in Figures 6b–6g. We analyze the simulated morphologies along the central plane of the computational domain; see Figure 6h. The intermediate steps during simulation of syntaxial quartz cementation (Figure 6i, at $t = 245$) resemble microstructural characteristics of the sandstone sample from North

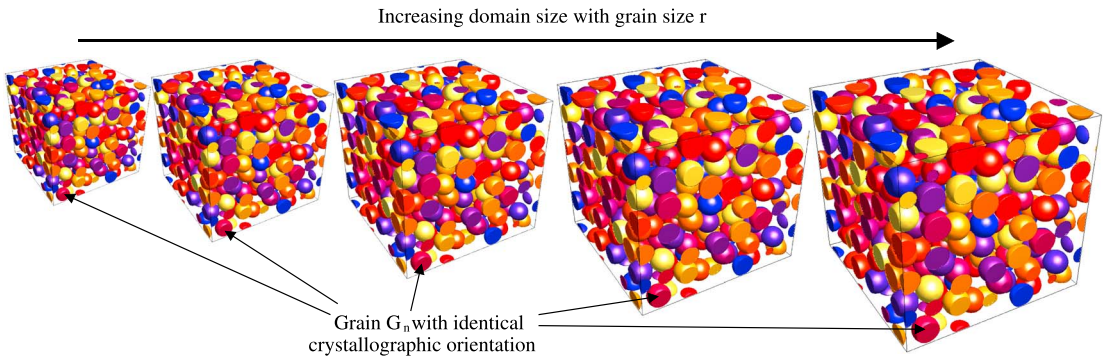

Figure 7. Geometrically similar computational domains with 265 randomly oriented grains, for different grain sizes. The crystallographic orientation of each grain G_n is kept the same for all domains.

England (Figures 1a and 1b) in terms of both the overgrowth facets and remaining pores. In particular, three characteristic similarities can be drawn as indicated in Figure 6i.

1. When sufficient pore space is available for syntaxial cementation, well-developed, flat facets (pyramidal or prismatic) form.
2. In the absence of sufficient pore space required for attaining the euhedral shape, constrained growth occurs due to interference of grain boundaries, resulting in randomly shaped grains.
3. The pore space along a thin section is occluded by the overgrowths progressing from the adjacent planes that can only be simulated by accounting for the third spatial dimension. The present simulation demonstrates the advantage of 3-D simulations over the previous studies that have been primarily limited to 2-D.

Furthermore, at later stages, the prismatic or pyramidal facets developed during cementation are no longer distinguishable in both the 3-D simulation (Figure 6j, at $t = 525$) and the 2-D thin section from rock samples of the Rotliegend sandstone sample from North Germany (Figures 1c and 1d). The model is capable of sufficiently recreating the development of quartz overgrowths, comparable to natural samples based on optical criteria and crystal morphologies.

3.2.3. Sealing Kinetics: Influence of Initial Grain Size

In order to derive the precise effect of initial grain size r on the sealing kinetics of quartz cementation, geometrically similar cubic computational domains comprising 265 grains ($G_1, \cdots, G_{265}$) of distinct randomly chosen crystallographic orientations (within each domain) were generated for five different grain sizes, as shown in Figure 7. Grain sizes and the corresponding dimension of the domains are listed in Table 3. Geometric similarity was achieved by scaling the position vector of each grain and edge length of simulation domain in proportion to different grain size. Further, in order to ensure identical influence of neighboring grains, the orientation of each grain G_n, $n \in \{1, \cdots, 265\}$, was kept the same in all the scaled domains, as illustrated in Figure 7. Algorithmically, the initial porosity in each domain is around 67%, which is higher than the observed porosities in sandstones at deposition (39–47% for eolian sediments, Schenk, 1981). However, we remark that the effect of initial grain size r, under the geometrically similar setting of simulation domains (for different values of r), can safely be extracted out of the study without significant effects of the initial porosity. As in the previous

Table 3
Numerical Values of Initial Grain Sizes r and the Corresponding Simulation Domain Sizes

Initial grain size r	Domain size
$20\Delta x$	$300\Delta x \times 300\Delta x \times 300\Delta x$
$25\Delta x$	$375\Delta x \times 375\Delta x \times 375\Delta x$
$30\Delta x$	$450\Delta x \times 450\Delta x \times 450\Delta x$
$35\Delta x$	$525\Delta x \times 525\Delta x \times 525\Delta x$
$40\Delta x$	$600\Delta x \times 600\Delta x \times 600\Delta x$

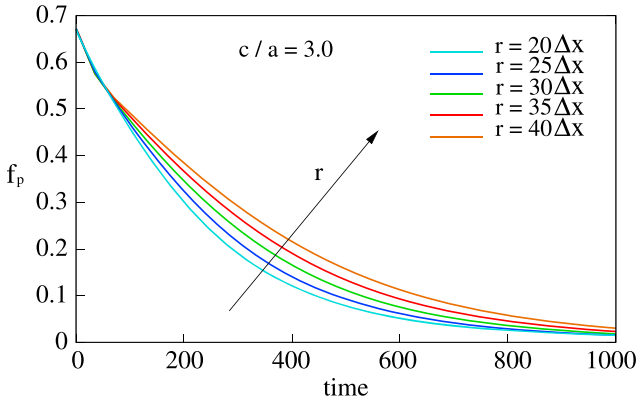

Figure 8. Plot of porosity f_p as a function of time for different values of initial grain size r. The rate of porosity loss is higher for fine grains and decreases with increase in initial grain size.

3-D simulation, the chemical driving force is assigned to be time invariant ($\Delta f_{g,l} = -0.3$). We plot the temporal evolution of porosity, characterized by volume fraction of liquid, for different values of r; see Figure 8. It is observed that the porosity-time curves is convex, which has also been suggested by Wangen (1998). Furthermore, the rate of porosity loss is inversely dependent on the initial grain size. This essentially implies that fine-grained samples get cemented at a faster rate compared to the coarser ones, as reported in experiments (Heald & Renton, 1966; Lander et al., 2008).

In order to comprehend the evolution of cemented microstructures, we analyze the interactions of six neighboring grains (namely, G_1, G_2, G_3, G_4, G_5, and G_6) in isolation with the rest, for $r = 20\Delta x$ (fine) and $r = 40\Delta x$ (coarse). The following characteristic differences are noted as also summarized in Figure 9.

1. At $t = 0$, the relative configuration of coarse and fine grains is identical.
2. At $t = 105$ (green outlet pictures), for fine grains, one noninteracting adjacent grain pair (G_5-G_6) is present. While for coarse grains two noninteracting adjacent grain pairs (G_3-G_4, G_5-G_6) are present.
3. At $t = 455$ (blue outlet pictures), fine grains form a closed loop, while coarse grains require further time steps to establish G_5-G_6 contact.
4. At $t = 1050$, closed loop is established for both fine and coarse grains leading to nearly similar grain configurations.

In order to compare the relative grain configuration for fine and coarse grain simulations, we introduce a measure, *similarity factor* ω, based on the work of Demirel et al. (2003) that computes the similarity between all the grid points from two separate numerical data of equal size and is given by

$$\omega = \frac{n_m}{n_t}, \tag{15}$$

where n_m and n_t denote the number of *matching* and *total* grid points, respectively. Therefore, an absolute match leads to $\omega = 1$ while a complete mismatch to $\omega = 0$. The size of numerical data for coarse grains is 8 times larger (2 times in each direction) than that for the finer grains. Therefore, every second grid point in each direction in the numerical domain of coarse grains is compared to that of every grid point in each direction in the domain of fine grains. We observe that starting from $\omega \approx 0.95$ at $t = 0$, the similarity factor drastically decreases reaching a minimum, which signifies a considerable difference in the sealing kinetics, as shown in the inset picture of Figure 9c. With further time steps, ω increases monotonically and tends toward 1, thereby, implying near similarity in the numerically cemented microstructures for fine and coarse grains. From the plots in Figures 8 and 9c, it is evident that the effect of initial grain size on the sealing kinetics is dominant during the intermediate stages but subsides during the later stages of cementation. The described sealing behavior in Figure 8 can be rationalized based on the arguments of unconstrained single crystal growth (in section 3.2.1). The additional complexities arising due to the grain boundary interactions do not influence the movement of grain-liquid interfaces. Therefore, although the kinetics may differ, the principal behavior of the sealing curve for finer grains lying below the coarser ones remains the same.

3.2.4. Influence of Cementation on Pore Size Distributions

We investigate the influence of progressive quartz cementation on the evolution of pore size distribution (PSD) in sandstone. For the phase-field simulation corresponding to $r = 20\Delta x$ (in section 3.2.3), 3-D pore space

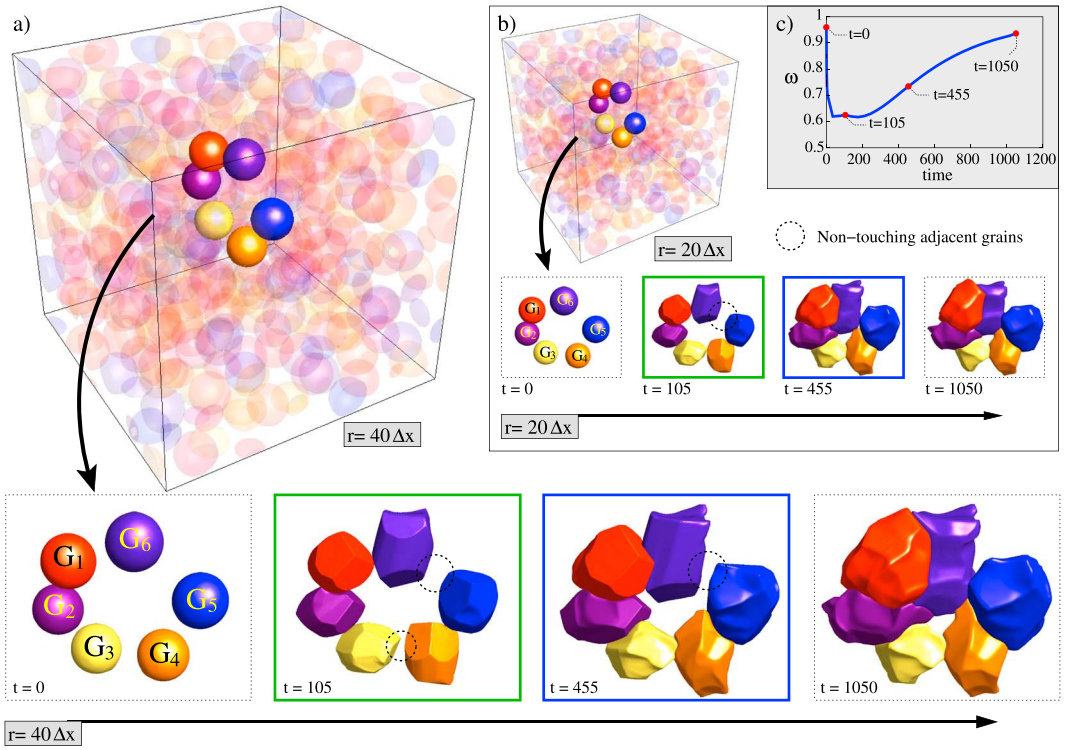

Figure 9. Temporal evolution of six grains among a distribution of 265 randomly oriented grains for (a) $r = 40\Delta x$ and (b) $r = 20\Delta x$. Progression is shown at representative time steps. Dotted circles represent the noninteracting adjacent grain pairs. Significant difference is observed between the corresponding green and blue outlet pictures of fine and coarse grain simulations. (c) Plot of similarity factor ω over time.

data were extracted at five representative time steps, as illustrated by different colored points in porosity-time plots in Figure 10a. For each pore space geometry, the medial axis transform was calculated using the post-processing tool chain of Pace3D (Hötzer et al., 2018; Pace3d, 2015). Thereby, each discretization grid point lying on the obtained medial axis was assigned a radius corresponding to the largest spherical pore that can be inserted into the pore space at that point. Based on the medial axis transform data, we estimate the PSDs locally. We plot the relative and cumulative pore size frequency distributions at different stages of numerically cemented pore space; see Figure 10b. The combined plots of smoothed relative and cumulative frequency distributions are depicted in Figure 10c. Distinct colors in Figures 10b and 10c correspond to different points on the porosity-time plot (values specified in the legend) in Figure 10a. For the initial pore space (at $t = 0$) that corresponds to spherical grains, the relative pore size frequency distribution is a *bell-shaped* curve. Netto (1993) reported that such a normal distribution is expected for clean and well-sorted sandstones. As the pore space reduces, at $t = 70$, the relative frequency distribution exhibits a bimodal behavior with the appearance of a second peak at lower pore radius, implying a considerable percentage of small-sized pores. Moreover, the first peak (at higher pore radius) shifts toward left indicating the reduction of overall pore sizes due to cementation. At subsequent stages ($t = 175, 315, 525$), the percentage of small-sized pores monotonically increases as also revealed by the cumulative frequency distributions (inset picture of Figure 10c). It is observed that the relative distribution evolves into an eventual lognormal kind of pattern at $t = 525$, generally exhibited by reservoir sandstones (Netto, 1993). Moreover, at same porosities, the pore size statistics for $r = 40\Delta x$ can be inferred by multiplying the pore radius scale for $r = 20\Delta x$ by a factor of 2 and accordingly for other initial grain sizes. Due to the geometric similarity of the computational domains in the presented set of simulations, the evolution of pore size frequency distributions will follow the same path as depicted in Figure 10b for different-sized grain packs, while the rates will vary inversely with initial grain size in accordance with the sealing kinetics.

3.2.5. Influence of Cementation on Permeability-Porosity Relationships

We investigate the influence of pore space cementation on the evolution of permeability using CFD analysis and compare the numerical results with an existing permeability model. From the phase-field simulations

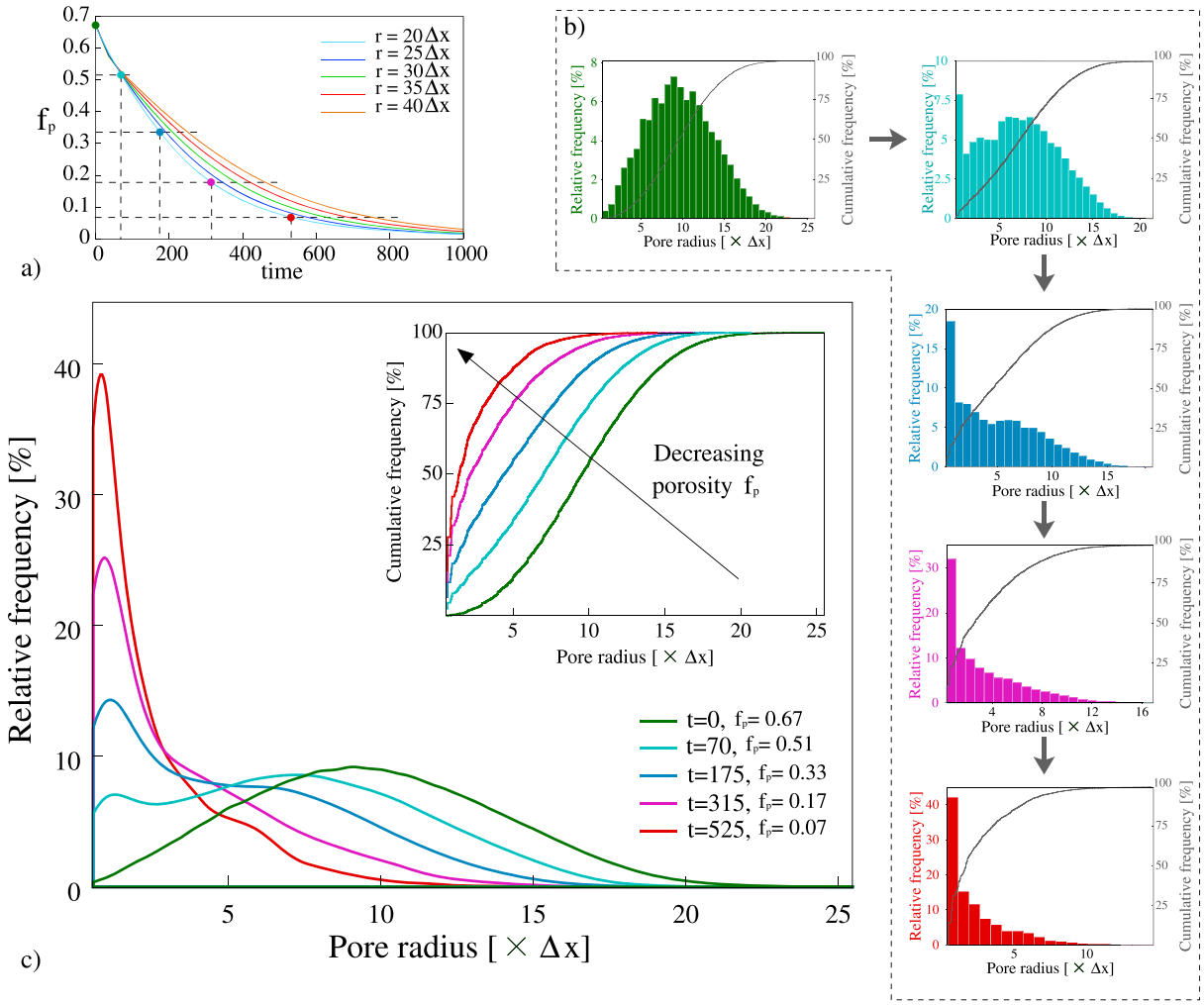

Figure 10. (a) Porosity-time plots illustrating five representative data points where pore space was analyzed for pore size distributions. (b) Temporal evolution of relative and cumulative pore size frequency distributions. The progression is shown at the chosen representative time steps. (c) Combined plots of smoothed relative and cumulative pore size frequency distributions. Distinct colors of plots in Figures 10b and 10c correspond to different points on the porosity-time plot in Figure 10a.

of quartz cementation reported in section 3.2.3, numerical data of 3-D pore space at successive time steps (for different grain sizes) were extracted. We simulate viscous fluid flow through the pore space in order to compute the numerical permeability of progressively sealed microstructures.

For every flow simulation, a constant pressure drop was prescribed (based on the free-stream boundary conditions in section 2.2) on the edges of simulation domain normal to *x* direction. The velocity field was computed based on the governing Stokes equations for incompressible fluids under laminar flow assumption and negligible body force, described in section 2.2. For the sake of convenience, the CFD simulation parameters (with

Table 4
Nondimensional and Dimensional Values of the Flow Parameters Used for CFD Analysis and Computation of Permeability

Parameter	Nondimensional value	Dimensional value
Pressure drop Δp	0.2	8 Pa
Dynamic viscosity μ	0.2	0.0010026 Pa s

Note. CFD = computational fluid dynamics.

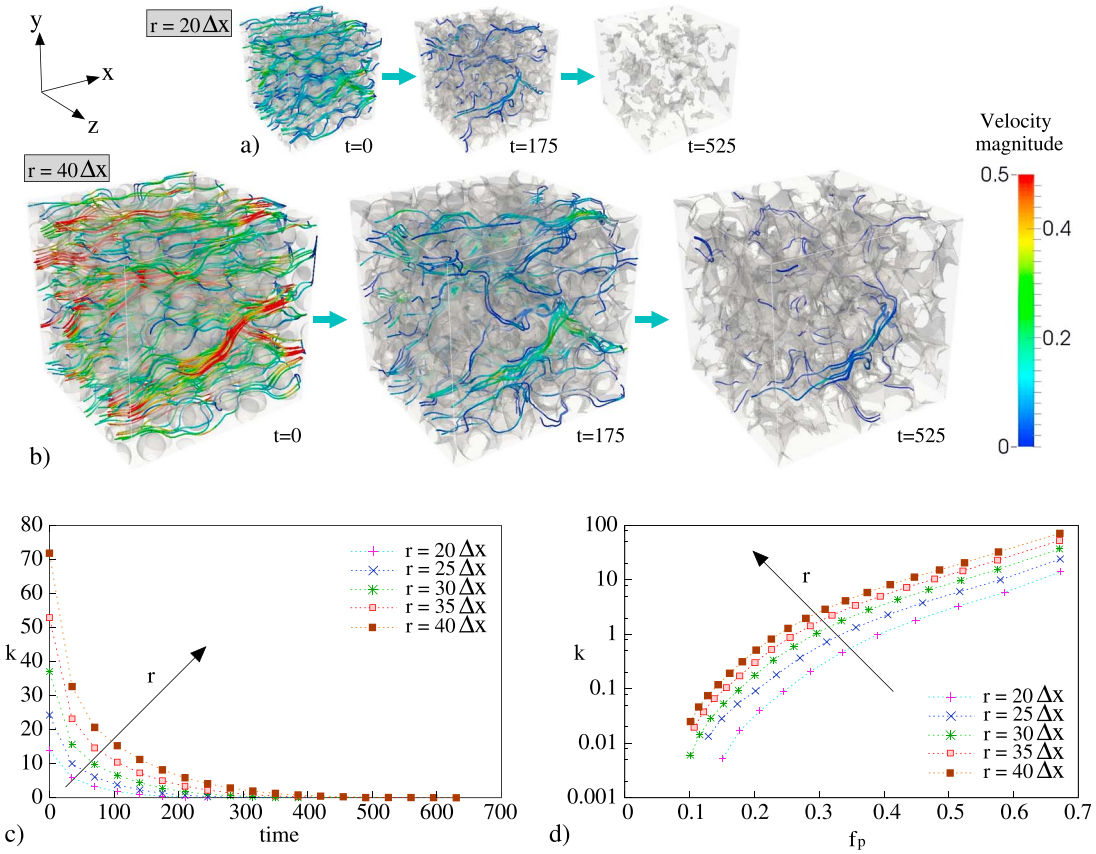

Figure 11. Velocity stream lines for different stages of cementation for (a) fine multigrain system ($r = 20\Delta x$) and (b) coarse multigrain system ($r = 40\Delta x$). The color map corresponds to the magnitude of velocity for systems in Figures 11a and 11b. (c) Plots of permeability k over time for different initial grain sizes r. (d) Permeability-porosity (k-f_p) relationship in semilog scale, for different values of r.

physical units) were nondimensionalized. The nondimensional values of the parameters are shown in column 2 of Table 4. For the length scale $l' = 1\mu m$ (same as that of phase-field simulations) and the fluid properties of water at 20 °C, we have the dynamic viscosity of $\mu = 0.0010026$ kg/m-s (Aleksandrov & Trakhtengerts, 1974) and density $\rho = 998.203$ kg/m^3 (Weast, 1972). For a chosen pressure drop $\Delta p = 8$ Pa in the x direction across the simulation domain, the resulting Reynolds numbers are close to 0.1 for the initial pore geometries and even lower for the subsequently cemented pore space, maintaining the laminar flow under Stokes' assumption. The dimensional values (with physical units) of the parameters used for the flow simulations are listed in column 3 of Table 4.

Exemplary velocity streamlines at different stages of cementation in multigrain systems with grain sizes $r = 20\Delta x$ and $r = 40\Delta x$ are depicted in Figures 11a and 11b, respectively. We observe that at every time step, the coarse-grained pack ($r = 40\Delta x$) exhibits higher fluid velocities (depicted by reddish streamlines) compared to fine pack ($r = 20\Delta x$). The temporal evolution of permeability (k) of numerically cemented

Table 5
Values Yielding Best Fit for the Numerically Obtained Permeability-Porosity Data With Power law Fitting

Grain size r	c	b
$20\Delta x$	106.35	5.08
$25\Delta x$	125.21	4.45
$30\Delta x$	193.27	4.36
$35\Delta x$	248.79	4.18
$40\Delta x$	312.16	4.05

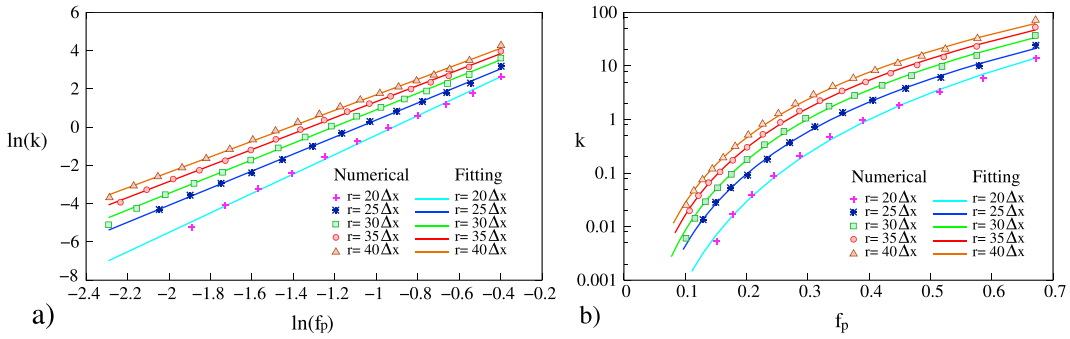

Figure 12. (a) Best fit generated by extracting the slope b and ordinate axis intercept ln [c] of linear curves in ln k-ln f_p scales. (b) Fitted curves (continuous lines) and the numerical data (discrete points) in semilog scale.

microstructures (calculated using equation (13) for different initial grain sizes is plotted in Figure 11c. The initial permeability of the fine multigrain system is lower in comparison to coarser ones due to larger volume of pore space in coarse-grained packs. Further, the permeability of finer packs diminishes earlier than coarser ones in response to cementation. Using the obtained temporal evolution of porosity (Figure 8) and permeability (Figure 11c), we derive the permeability-porosity (k-f_p) relationships for different grain sizes, in Figure 11d. Based on the chosen length scale (in column 3 of Table 1), the obtained permeabilities in all the simulations lie in the range of 5 mD to 7.2 $\times$ 10^4 mD. Experimentally established permeability-porosity behavior (Füchtbauer, 1988) shows that at same porosity, coarser sands are more permeable than fine-grained ones. The k-f_p relationships obtained from phase-field simulations (in Figure 11d) are in qualitative agreement with previous experimental investigations. In a similar way, a relationship between permeability and PSDs can be inferred, from the values of porosity in Figures 10 and 11d.Mathematical models such as *Kozeny-Carman* equations and Timur's model are convenient tools of permeability estimation from well logs and log-derived data, in the absence of core measurements. While certain quantities (e.g., porosity and irreducible water saturation) can be conventionally estimated from well logs, analytical techniques for determining values of specific surface area and mean grain size from the well-log data have also been proposed (e.g., Salem & Chilingarian, 1999). A wide spectrum of predictive models correlating permeability with porosity and other physical rock parameters (such as irreducible water saturation, mean grain size, sorting, and surface area) has been proposed by petrophysicists, based on their analysis of experimental data of natural samples from various geological settings (see ; Nelson et al., 1994, for a detailed review on permeability models). Several models (including the aforementioned Timur's model) suggest a power law relationship between permeability and porosity with additional physical parameters.

Therefore, we employ a power law fitting ($k = cf_p^b$) for our numerically obtained permeability-porosity trends. We find that the best fit (for different grain sizes) is achieved for the values of fitting parameters (c and b) summarized in Table 5. Exponent b is determined from the numerical data by plotting ln k versus ln f_p and extracting the slope of the fitted curve for different grain sizes. The results are displayed in Figure 12a. The fitted curves along with the numerical data in semilog scale are depicted in Figure 12b. In Timur's model (Timur, 1968), which is given by

$$k = \frac{af_p^b}{S_{wi}^2}, \tag{16}$$

the permeability k is correlated with porosity f_p, irreducible water saturation S_{wi}, and two empirical parameters a and b. Timur's statistical results indicate that exponent b varies between 3 and 5 depending upon the data and still produce reasonably good fits. Although S_{wi} cannot be constrained separately within the present approach, it is reasonable to assume that the power law behavior is still valid. Further, it is worth mentioning that the obtained exponents (in column 3 of Table 5) fall within the range proposed by Timur.

4. Concluding Remarks

Present work demonstrates the capabilities of the multiphase-field model in capturing several aspects of diagenetic process of syntaxial quartz cementation. Numerical experiments of unitaxial growth in fractures indicate the formation of bridge structures for crystals with a c/a ratio of 3.0 that is consistent with the experiments of Lander et al. (2008) and Okamoto and Sekine (2011). Moreover, 3-D phase-field simulations of

cementation in sandstone with the calibrated value of *c*/*a* ratio were successful in reproducing natural crystal morphologies and size effects as enumerated below.

1. Simulations of undisturbed cement growth indicate that fine grains develop their euhedral form faster compared to coarser ones, as reported in experiments (Lander et al., 2008).
2. Simulations of constrained growth in multigrain system signify the following characteristic similarities of the numerically cemented grains (visualized along central plane of 3-D domain) with the natural thin sections of Busch et al. (2017):
    a. Flat facets (euhedral form) are developed when enough space is available for syntaxial overgrowth cementation.
    b. Randomly shaped grains are formed due to constrained growth when sufficient space in not present.
    c. Grains appear from adjacent planes (which further advocates the advantage of 3-D numerical studies over 2-D simulations).
3. Simulations of different-sized multigrain systems indicate two important aspects about kinetics of pore space sealing:
    a. The nonlinear porosity-time curve for each grain size *r* is convex with respect to time, as suggested by Wangen (1998).
    b. The rate of porosity loss in finer grain packs is larger than that in coarser ones. This signifies faster cementation of finer sands that is in agreement with the experimental works of Heald and Renton (1966) and Lander et al. (2008).
4. The analysis of pore size statistics at different stages of cementation reveals that the relative frequency distribution evolves from bell-shaped curve to lognormal patterns.
5. CFD analysis performed on the numerically cemented microstructures for computing the permeability at different stages of cementation reveals two important aspects of the obtained permeability-porosity relationships:
    a. Coarse sands possessing the same porosity as finer ones have a comparatively larger permeability that is in agreement with the published literature (e.g., Füchtbauer, 1988).
    b. Permeability-porosity curves follow a power law relationship with exponents lying between 3 and 5, as suggested by empirical equations of Timur (1968).

The present modeling approach assumes a constant driving force for the crystallization, which implies that the fluid is continuously being replenished, thereby maintaining a constant solute concentration. Wendler et al. (2015) discussed the physical conditions where the aforementioned assumption is admissible by evaluating the Reynolds number (*Re*), Peclet number (*Pe*), and Damköhler number of second kind (Da_{II}), using real experimental data pertaining to quartz growth, and demonstrated that the conditions are sufficiently realized under their growth conditions (see ; Okamoto et al., 2010; Okamoto & Sekine, 2011). However, within the isolated pores, as the solute transport is prevented, such conditions (i.e., invariant solute concentration with time) cannot be met. Further, in a system where solute is not replenished with progressive crystallization, the cement growth rates will continuously decrease. Hence, for a complete treatment of the process, the present approach should be extended by coupling with diffusion and flow equations.

Acknowledgments
N. P., M. S., and B. N. are thankful to the Helmholtz Association for financial support through the program EMR-Energy efficiency, Materials and Resources and KIT-geothermal integration initiative within the program RE-renewable energies. K. A. acknowledges the financial support from the College of Engineering, Arizona State University. Further, the authors would like to state that no new data were used in producing this manuscript.

References

Ajdukiewicz, J. M., & Lander, R. H. (2010). Sandstone reservoir quality prediction: The state of the art. *AAPG Bulletin*, *94*(8), 1083–1091.

Aleksandrov, A., & Trakhtengerts, M. (1974). Viscosity of water at temperatures of −20 to 150 °C. *Journal of Engineering Physics and Thermophysics*, *27*(4), 1235–1239.

Amthor, J. E., & Okkerman, J. (1998). Influence of early diagenesis on reservoir quality of Rotliegende sandstones, northern Netherlands. *AAPG Bulletin*, *82*(12), 2246–2265.

Ankit, K., Nestler, B., Selzer, M., & Reichardt, M. (2013). Phase-field study of grain boundary tracking behavior in crack-seal microstructures. *Contributions to Mineralogy and Petrology*, *166*(6), 1709–1723.

Ankit, K., Selzer, M., Hilgers, C., & Nestler, B. (2015). Phase-field modeling of fracture cementation processes in 3-D. *Journal of Petroleum Science Research*, *4*, 2168–5517.

Ankit, K., Urai, J. L., & Nestler, B. (2015). Microstructural evolution in bitaxial crack-seal veins: A phase-field study. *Journal of Geophysical Research: Solid Earth*, *120*, 3096–3118. https://doi.org/10.1002/2015JB011934

Auzerais, F., Dunsmuir, J., Ferreol, B., Martys, N., Olson, J., Ramakrishnan, T., et al. (1996). Transport in sandstone: A study based on three dimensional microtomography. *Geophysical Research Letters*, *23*(7), 705–708.

Bernabé, Y., Mok, U., & Evans, B. (2003). Permeability-porosity relationships in rocks subjected to various evolution processes. *Pure and Applied Geophysics*, *160*(5), 937–960.

Bjørkum, P. A., Oelkers, E. H., Nadeau, P. H., Walderhaug, O., & Murphy, W. M. (1998). Porosity prediction in quartzose sandstones as a function of time, temperature, depth, stylolite frequency, and hydrocarbon saturation. *AAPG Bulletin*, *82*(4), 637–648.

Bjorlykke, K., & Egeberg, P. (1993). Quartz cementation in sedimentary basins. *AAPG Bulletin*, *77*(9), 1538–1548.

Bjørlykke, K., & Jahren, J. (2015). Sandstones and sandstone reservoirs. In *Petroleum Geoscience* (pp. 119 – 149). Springer.
Blunt, M. J., Bijeljic, B., Dong, H., Gharbi, O., Iglauer, S., Mostaghimi, P., et al. (2013). Pore-scale imaging and modelling. *Advances in Water Resources*, *51*, 197 – 216.
Bons, P. (2001). Development of crystal morphology during unitaxial growth in a progressively widening vein: I. The numerical model. *Journal of Structural Geology*, *23*(6), 865 – 872.
Bosl, W. J., Dvorkin, J., & Nur, A. (1998). A study of porosity and permeability using a lattice Boltzmann simulation. *Geophysical Research Letters*, *25*(9), 1475 – 1478.
Busch, B., Hilgers, C., Gronen, L., & Adelmann, D. (2017). Cementation and structural diagenesis of fluvio-aeolian Rotliegend sandstones, Northern England. *Journal of the Geological Society*, *174*, 855 – 868.
Busch, B., Hilgers, C., Lander, R. H., Bonnell, L. M., & Adelmann, D. (2018). Reservoir quality and burial model evaluation by kinetic quartz and illite cementation modeling: Case study of Rotliegendes, North Germany. *AAPG Bulletin*, *102*(2), 293 – 307.
Canals, M., & Meunier, J. D. (1995). A model for porosity reduction in quartzite reservoirs by quartz cementation. *Geochimica et Cosmochimica Acta*, *59*(4), 699 – 709.
Chen, L.-Q. (2002). Phase-field models for microstructure evolution. *Annual Review of Materials Research*, *32*(1), 113 – 140.
Demirel, M., Kuprat, A., George, D., & Rollett, A. (2003). Bridging simulations and experiments in microstructure evolution. *Physical Review Letters*, *90*, 016106.
Deng, S., Zuo, L., Aydin, A., Dvorkin, J., & Mukerji, T. (2015). Permeability characterization of natural compaction bands using core flooding experiments and three-dimensional image-based analysis: Comparing and contrasting the results from two different methods. *AAPG Bulletin*, *99*(1), 27 – 49.
dos Anjos, S. M., De Ros, L. F., de Souza, R. S., de Assis Silva, C. M., & Sombra, C. L. (2000). Depositional and diagenetic controls on the reservoir quality of Lower Cretaceous Pendencia sandstones, Potiguar rift basin, Brazil. *AAPG bulletin*, *84*(11), 1719 – 1742.
Dutton, S. P., Loucks, R. G., & Day-Stirrat, R. J. (2012). Impact of regional variation in detrital mineral composition on reservoir quality in deep to ultradeep lower Miocene sandstones, western Gulf of Mexico. *Marine and Petroleum Geology*, *35*(1), 139 – 153.
Feng, L., Feng, X.-j., Lu, Y., Zhu, C.-s., & Jia, B.-b. (2017). Phase field modeling of lamellar eutectic growth under the influence of fluid flow. *Computational Materials Science*, *137*, 171 – 178.
Frondel, C. (1962). *Dana's system of mineralogy, Vol. 3, silica minerals* (7th ed.). New York: John Wiley.
Füchtbauer, H. (1988). *Sandsteine, Sedimente und Sedimentgesteine* (4th ed., pp. 94 – 187): Stuttgart, Germany: Schweizerbart.
Harlow, F. H., & Welch, J. E. (1965). Numerical calculation of time-dependent viscous incompressible flow of fluid with free surface. *The Physics of Fluids*, *8*(12), 2182 – 2189.
Heald, M., & Renton, J. (1966). Experimental study of sandstone cementation. *Journal of Sedimentary Research*, *36*(4), 977 – 991.
Hilgers, C., Koehn, D., Bons, P., & Urai, J. (2001). Development of crystal morphology during unitaxial growth in a progressively widening vein: II. Numerical simulations of the evolution of antitaxial fibrous veins. *Journal of Structural Geology*, *23*(6), 873 – 885.
Hötzer, J., Reiter, A., Hierl, H., Steinmetz, P., Selzer, M., & Nestler, B. (2018). The parallel multi-physics phase-field framework Pace3d. *Journal of Computational Science*, *26*, 1 – 12.
Kling, T., Schwarz, J.-O., Wendler, F., Enzmann, F., & Blum, P. (2017). Fracture flow due to hydrothermally induced quartz growth. *Advances in Water Resources*, *107*, 93 – 107.
Koehn, D., Hilgers, C., Bons, P. D., & Passchier, C. W. (2000). Numerical simulation of fibre growth in antitaxial strain fringes. *Journal of Structural Geology*, *22*(9), 1311 – 1324.
Lander, R. H., Larese, R. E., & Bonnell, L. M. (2008). Toward more accurate quartz cement models: The importance of euhedral versus noneuhedral growth rates. *AAPG Bulletin*, *92*(11), 1537 – 1563.
Lander, R., & Laubach, S. (2015). Insights into rates of fracture growth and sealing from a model for quartz cementation in fractured sandstones. *Geological Society of America Bulletin*, *127*(3-4), 516 – 538.
Lander, R. H., & Walderhaug, O. (1999). Predicting porosity through simulating sandstone compaction and quartz cementation. *AAPG Bulletin*, *83*(3), 433 – 449.
Laubach, S., Reed, R., Olson, J., Lander, R., & Bonnell, L. (2004). Coevolution of crack-seal texture and fracture porosity in sedimentary rocks: Cathodoluminescence observations of regional fractures. *Journal of Structural Geology*, *26*(5), 967 – 982.
Ma, J. (2015). Review of permeability evolution model for fractured porous media. *Journal of Rock Mechanics and Geotechnical Engineering*, *7*(3), 351 – 357.
Marchand, A. M., Haszeldine, R. S., Smalley, P. C., Macaulay, C. I., & Fallick, A. E. (2001). Evidence for reduced quartz-cementation rates in oil-filled sandstones. *Geology*, *29*(10), 915 – 918.
Moelans, N., Blanpain, B., & Wollants, P. (2008). An introduction to phase-field modeling of microstructure evolution. *Calphad*, *32*(2), 268 – 294.
Nelson, P. H., et al. (1994). Permeability-porosity relationships in sedimentary rocks. *The Log Analyst*, *35*(03), 38 – 62.
Nestler, B., & Choudhury, A. (2011). Phase-field modeling of multi-component systems. *Current Opinion in Solid State and Materials Science*, *15*(3), 93 – 105.
Nestler, B., Garcke, H., & Stinner, B. (2005). Multicomponent alloy solidification: Phase-field modeling and simulations. *Physical Review E*, *71*(4), 041609.
Nestler, B., Wendler, F., Selzer, M., Stinner, B., & Garcke, H. (2008). Phase-field model for multiphase systems with preserved volume fractions. *Physical Review E*, *78*(1), 011604.
Netto, A. (1993). Pore-size distribution in sandstones. *AAPG Bulletin*, *77*(6), 1101 – 1104.
Oelkers, E. H., Bjørkum, P., & Murphy, W. M. (1996). A petrographic and computational investigation of quartz cementation and porosity reduction in North Sea sandstones. *American Journal of Science*, *296*(4), 420 – 452.
Okamoto, A., Saishu, H., Hirano, N., & Tsuchiya, N. (2010). Mineralogical and textural variation of silica minerals in hydrothermal flow-through experiments: Implications for quartz vein formation. *Geochimica et Cosmochimica Acta*, *74*(13), 3692 – 3706.
Okamoto, A., & Sekine, K. (2011). Textures of syntaxial quartz veins synthesized by hydrothermal experiments. *Journal of Structural Geology*, *33*(12), 1764 – 1775.
Øren, P.-E., & Bakke, S. (2002). Process based reconstruction of sandstones and prediction of transport properties. *Transport in Porous Media*, *46*(2-3), 311 – 343.
Pace3d (2015). Parallel Algorithm for Crystal evolution in 3-D. Retrieved from https://www.hs-karlsruhe.de/idm/pace3d-software/
Paxton, S., Szabo, J., Ajdukiewicz, J., & Klimentidis, R. (2002). Construction of an intergranular volume compaction curve for evaluating and predicting compaction and porosity loss in rigid-grain sandstone reservoirs. *AAPG Bulletin*, *86*(12), 2047 – 2067.
Plapp, M. (2012). Phase-field models. In *Multiphase micro uidics: The diffuse interface model* (pp. 129 – 175). Springer.

Prajapati, N., Selzer, M., & Nestler, B. (2017). Computational modeling of calcite cementation in saline limestone aquifers: A phase-field study. *Geothermal Energy*, *5*(1), 15.
Prajapati, N., Selzer, M., Nestler, B., Busch, B., & Hilgers, C. (2018). Modeling fracture cementation processes in calcite limestone: A phase-field study. *Geothermal Energy*, *6*(1), 7.
Qin, R., & Bhadeshia, H. (2010). Phase field method. *Materials Science and Technology*, *26*(7), 803–811.
Rannacher, R. (2008). Methods for numerical flow simulation. *Hemodynamical Flows*, *37*, 275–332.
Rykart, R. (1995). Quarz-Monographie–Die Eigenheiten von Bergkristall, Rauchquarz, Amethyst, Chalcedon, Achat, Opal und anderen Varietäten.
Salem, H. S., & Chilingarian, G. V. (1999). Determination of specific surface area and mean grain size from well-log data and their influence on the physical behavior of offshore reservoirs. *Journal of Petroleum Science and Engineering*, *22*(4), 241–252.
Schenk, C. J. (1981). Porosity and textural characteristics of eolian stratification. *AAPG Bulletin*, *65*(5), 986–986.
Sliaupa, S. (2010). Predicting porosity through simulating quartz cementation of Middle Cambrian sandstones, West Lithuania. *Geological Quarterly*, *50*(2), 247–256.
Spanne, P., Thovert, J., Jacquin, C., Lindquist, W., Jones, K., & Adler, P. (1994). Synchrotron computed microtomography of porous media: Topology and transports. *Physical Review Letters*, *73*(14), 2001–2004.
Stinner, B., Nestler, B., & Garcke, H. (2004). A diffuse interface model for alloys with multiple components and phases. *SIAM Journal on Applied Mathematics*, *64*(3), 775–799.
Taylor, T. R., Kittridge, M. G., Winefield, P., Bryndzia, L. T., & Bonnell, L. M. (2015). Reservoir quality and rock properties modeling—Triassic and Jurassic sandstones, Greater Shearwater Area, UK Central North Sea. *Marine and Petroleum Geology*, *65*, 1–21.
Taylor, T., Stancliffe, R., Macaulay, C., & Hathon, L. (2004). High temperature quartz cementation and the timing of hydrocarbon accumulation in the Jurassic Norphlet Sandstone, offshore Gulf of Mexico, USA. *Geological Society, London, Special Publications*, *237*(1), 257–278.
Thiry, M., & Maréchal, B. (2001). Development of tightly cemented sandstone lenses in uncemented sand: Example of the Fontainebleau Sand (Oligocene) in the Paris Basin. *Journal of Sedimentary Research*, *71*(3), 473–483.
Timur, A. (1968). An investigation of permeability, porosity, and residual water saturation relationships. In *SPWLA 9th annual logging symposium*. Society of Petrophysicists and Well-Log Analysts.
Ukar, E., Laubach, S. E., & Marrett, R. (2016). Quartz *c* axis orientation patterns in fracture cement as a measure of fracture opening rate and a validation tool for fracture pattern models. *Geosphere*, *12*(2), 400–438.
Vondrous, A., Reichardt, M., & Nestler, B. (2014). Growth rate distributions for regular two-dimensional grains with Read–Shockley grain boundary energy. *Modelling and Simulation in Materials Science and Engineering*, *22*(2), 025014. 13pp.
Walderhaug, O. (1994a). Precipitation rates for quartz cement in sandstones determined by fluid-inclusion microthermometry and temperature-history modeling. *Journal of Sedimentary Research*, *64*(2), 324–333.
Walderhaug, O. (1994b). Temperatures of quartz cementation in Jurassic sandstones from the Norwegian continental shelf—Evidence from fluid inclusions. *Journal of Sedimentary Research*, *64*(2), 311–323.
Walderhaug, O. (1996). Kinetic modeling of quartz cementation and porosity loss in deeply buried sandstone reservoirs. *AAPG Bulletin*, *80*(5), 731–745.
Walderhaug, O. (2000). Modeling quartz cementation and porosity in Middle Jurassic Brent Group sandstones of the KvitebjØfield, northern North Sea. *AAPG Bulletin*, *84*(9), 1325–1339.
Wang, F., Choudhury, A., Selzer, M., Mukherjee, R., & Nestler, B. (2012). Effect of solutal Marangoni convection on motion, coarsening, and coalescence of droplets in a monotectic system. *Physical Review E*, *86*(6), 066318.
Wangen, M. (1998). Modeling porosity evolution and cementation of sandstones. *Marine and Petroleum Geology*, *15*(5), 453–465.
Wangen, M. (1999). Modelling quartz cementation of quartzose sandstones. *Basin Research*, *11*, 113–126.
Waugh, B. (1970). Formation of quartz overgrowths in the Penrith Sandstone (Lower Permian) of northwest England as revealed by scanning electron microscopy. *Sedimentology*, *14*(3-4), 309–320.
Weast, R. C. (1972). *Handbook of chemistry and physics 53rd edition*. Cleveland, OH: Chemical Rubber Pub.
Wendler, F., Okamoto, A., & Blum, P. (2015). Phase-field modeling of epitaxial growth of polycrystalline quartz veins in hydrothermal experiments. *Geofluids*, *16*, 211–230.
Worden, R., & Burley, S. (2003). Sandstone diagenesis: The evolution of sand to stone. *Sandstone Diagenesis: Recent and Ancient*, *4*, 3–44.
Worden, R., & Morad, S. (2000). Quartz cementation in oil field sandstones: A review of the key controversies, quartz cementation in sandstones. *International Association of Sedimentologists Special Publication*, *29*, 1–20.
Zhang, J., & Adams, J. B. (2002). FACET: A novel model of simulation and visualization of polycrystalline thin film growth. *Modelling and Simulation in Materials Science and Engineering*, *10*(4), 381–401.